ICAS 2021 SHANGHAI
International Council of the Aeronautical Sciences
32nd Congress of the International Council of the Aeronautical Sciences
September 6-10, 2021
Pudong Shangri-La, Shanghai, China

PHISICAL AND MATHEMATICAL MODELS OF THE BUFFET ONSET

Lipanov A.M.[1], Lipatov I.I.[2], Karskanov S.A.[3]

[1]Keldysh Institute of Applied Mathematics Russian Academy of Sciences, Moscow, Russia
[2]Central Aerohydrodynamic Institute, Zhukovsky, Russia
[3]Udmurt Federal Research Center of the Ural Branch of the Russian Academy of Sciences, Izhevsk, Russia

Abstract

The phenomenon of the high-speed buffet onset is investigated when a transonic flow is flown around the NACA0012 airfoil. A mathematical model based on high-order approximation algorithms is proposed, which allows calculating unsteady separated flows. The model is formed on the integration of quasi-hydrodynamic equations. A parametric study of the high-speed viscous gas flow around the airfoil is carried out, depending on the angle of attack. Both instantaneous and averaged flow patterns are analyzed. Pulsation of flow characteristics distributions at different attack angles are obtained. The regularities of the boundary layer separation occurrence are revealed. The shock waves influence on the flow regime near the airfoil surface is determined. The critical attack angle of high-speed buffet onset is determined.

Keywords: buffet, shock waves, quasi-gasdynamic equations, high-order approximation

1. Introduction

The buffet phenomenon attracted the attention of aerodynamicists in the 1930s after causing a number of plane crashes. It consists in the occurrence of forced the aircraft parts vibrations. However, it is worth distinguishing between landing and high-speed buffet. Landing buffet consists of the formation of a turbulent wake behind the bluff elements that vibrates parts of the aircraft.

The nature of high-speed buffet is associated with completely different physical phenomena. The phenomenon of high-speed buffet has been observed experimentally for a long time. When flying at high subsonic speeds, due to the wave crisis onset in the flow around the wing, the flow breaks down behind the shock wave. The flow mode changes sharply, and strong vibration occurs. High-speed buffet is more dangerous than landing.

A detailed study of this phenomenon, including the use of control actions on the buffet process, with the Reynolds averaging hypothesis, was carried out in [1]. In this paper, a similar problem is solved on the basis of direct numerical simulation. The quasi-gasdynamic (QGD) equations obtained by solving the Boltzmann kinetic equation [2, 3] are integrated.

A significant difference and feature of the QGD approach is the use of the spatio-temporal averaging procedure to determine the main gas-dynamic quantities (velocity, density, and pressure). Additional time smoothing caused the appearance of additional dissipative terms in the equations, which formally distinguish the QGD system from the Navier-Stokes system. The influence of additional terms is insignificant for stationary and quasi-stationary gas-dynamic flows. However, for strongly unsteady flows, as well as for Knudsen numbers close to unity, their contribution becomes significant. In numerical simulations additional terms manifest themselves as effective regulators. It is important that additional dissipative terms of the QGD equations do not cause a boundary layer effect. Thus, the QGD model solution does not fundamentally differ from the solution obtained using the Navier – Stokes equations. This is confirmed by numerous comparisons of calculation data [4]. The point of applying the QGD equations is that these systems are correct in their physical construction, since there is a minimum spatial (temporal) size at which strong changes in parameters can occur. For the Navier-Stokes equations, there are well-known difficulties in substantiating their correctness.

The presence of internal correctness determined the application success of the QGD equations for modeling the most complex unsteady viscous gas flows, problems of aeroacoustics and aerodynamics. This is precisely the advantage of this model.

2. Problem Statement

2.1 The Quasi-gasdynamic Equations System

A two-dimensional case was considered. The following QGD equations system was solved:

$$\frac{\partial \rho}{\partial t} + \frac{\partial j_x}{\partial x} + \frac{\partial j_y}{\partial y} = 0, \tag{1}$$

$$\frac{\partial (\rho u_x)}{\partial t} + \frac{\partial (j_x u_x)}{\partial x} + \frac{\partial (j_y u_x)}{\partial y} + \frac{\partial p}{\partial x} = \frac{\partial \Pi_{xx}}{\partial x} + \frac{\partial \Pi_{yx}}{\partial y}, \tag{2}$$

$$\frac{\partial (\rho u_y)}{\partial t} + \frac{\partial (j_x u_y)}{\partial x} + \frac{\partial (j_y u_y)}{\partial y} + \frac{\partial p}{\partial y} = \frac{\partial \Pi_{xy}}{\partial x} + \frac{\partial \Pi_{yy}}{\partial y}, \tag{3}$$

$$\frac{\partial (\rho E)}{\partial t} + \frac{\partial (j_x H)}{\partial x} + \frac{\partial (j_y H)}{\partial y} + \frac{\partial q_x}{\partial x} + \frac{\partial q_y}{\partial y} = \frac{\partial}{\partial x}\left(\Pi_{xx} u_x + \Pi_{xy} u_y\right) + \frac{\partial}{\partial y}\left(\Pi_{yx} u_x + \Pi_{yy} u_y\right). \tag{4}$$

Here, ρ was the density, p was the pressure, u_x and u_y were the components of the gas velocity vector, E was relative energy per unit gas mass, H was total relative enthalpy per unit gas mass, determined by the formula

$$H = E + p/\rho$$

The components of the flow density vector were calculated as follows:

$$j_x = \rho(u_x - w_x), \qquad j_y = \rho(u_y - w_y),$$

where

$$w_x = \frac{\tau}{\rho}\left(\frac{\partial (\rho u_x^2)}{\partial x} + \frac{\partial (\rho u_x u_y)}{\partial y} + \frac{\partial p}{\partial x}\right), \quad w_y = \frac{\tau}{\rho}\left(\frac{\partial (\rho u_x u_y)}{\partial x} + \frac{\partial (\rho u_y^2)}{\partial y} + \frac{\partial p}{\partial y}\right).$$

The viscous stress tensor components were determined using the expressions:

$$\Pi_{xx} = \Pi_{xx}^{NS} + u_x w_x^* + R^*, \qquad \Pi_{xy} = \Pi_{xy}^{NS} + u_x w_y^*,$$

$$\Pi_{yx} = \Pi_{yx}^{NS} + u_x w_x^*, \qquad \Pi_{yy} = \Pi_{yy}^{NS} + u_y w_y^* + R^*.$$

Here, $\Pi_{xx}^{NS}, \Pi_{xy}^{NS}, \Pi_{yx}^{NS}, \Pi_{yy}^{NS}$ were the viscous stress tensor components in the classical equations of hydromechanics (Navier-Stokes). Variables w_x^*, w_y^* R^* were calculated using the formulas:

$$w_x^* = \tau\left(\rho u_x \frac{\partial u_x}{\partial x} + \rho u_y \frac{\partial u_x}{\partial y} + \frac{\partial p}{\partial x}\right), \quad w_y^* = \tau\left(\rho u_x \frac{\partial u_y}{\partial x} + \rho u_y \frac{\partial u_y}{\partial y} + \frac{\partial p}{\partial y}\right),$$

$$R^* = \tau\left(u_x \frac{\partial p}{\partial x} + u_y \frac{\partial p}{\partial y} + kp \ \mathrm{div}\vec{u}\right).$$

The heat flux vector components were calculated by the formulas:

$$q_x = q_x^F - u_x R^q, \quad q_y = q_y^F - u_y R^q.$$

Here q_x and q_y were the Fourier components, and R^q was determined by the expression:

$$R^q = \tau\rho\left[\frac{u_x}{k-1}\frac{\partial}{\partial x}\left(\frac{p}{\rho}\right) + \frac{u_y}{k-1}\frac{\partial}{\partial y}\left(\frac{p}{\rho}\right) + p u_x \frac{\partial}{\partial x}\left(\frac{1}{\rho}\right) + p u_y \frac{\partial}{\partial y}\left(\frac{1}{\rho}\right)\right].$$

The equation of ideal gas state was used to close system (1-4).

To calculate the relaxation parameter, the expression

$$\tau = \frac{\mu}{p\,\mathrm{Sc}} \tag{5}$$

was used, where μ was the gas viscosity and Sh was the dimensionless Schmidt number.

QGD equations differ from the classical phenomenological equations of hydromechanics by the presence of gradients from additional terms w_x, w_y, w_x^*, w_y^*, R^*, R^q. As a result, these terms represent the second spatial derivatives of the gas density, the flow velocity vector components and pressure, being dissipative. All expressions corresponding to them were proportional to the relaxation parameter. It can be seen from expression (5) that with the pressure value increase the relaxation parameter becoming infinitesimally and when τ is equal to zero the classical equations of hydromechanics are obtained.

The system of equations (1-4) was solved according to an explicit difference scheme. The total variation diminishing Runge-Kutta scheme of the second order of accuracy was used [5]. Spatial derivatives were calculated with a high-order approximation WENO schemes [6].

2.2 Boundary Conditions

Nonreflecting boundary conditions were used at the open boundaries of the computational domain [7]. At the computational domain inlet, the equalities were set:

$$\frac{p}{\rho^k}=\frac{p_\infty}{\rho_\infty^{\,k}},\quad \frac{\partial p}{\partial t}-(c-u_x)\frac{\partial p}{\partial x}=0,\quad u_x+\frac{2c}{k-1}=u_{x\infty}+\frac{2c_\infty}{k-1},\quad u_y=u_{y\infty},$$

where the subscript "∞" denotes the parameters to the left of the input boundary. Here c was sonic speed.

At the computational domain outlet, a system of relations was used:

$$\frac{\partial \rho}{\partial t}+u_x\frac{\partial \rho}{\partial x}+\frac{1}{c}\frac{\partial p}{\partial x}=0,\quad \frac{\partial p}{\partial t}+(c+u_x)\frac{\partial p}{\partial x}=0,$$

$$\frac{\partial u_x}{\partial t}-(c+u_x)\frac{\partial u_x}{\partial x}=\alpha_1|u_{x\infty}-u_x|(u_{x\infty}-u_x),\quad \frac{\partial u_y}{\partial t}+u_x\frac{\partial u_y}{\partial x}=0,$$

where α_1 was the coefficient, the value of which was taken to be equal to one when performing the calculations.

On the upper bound, free stream condition was used:

$$\frac{\partial \mathbf{W}}{\partial t}+(c+u_y)\frac{\partial \mathbf{W}}{\partial y}=0,$$

where **W** was an algebraic vector $\mathbf{W}=(u_x,u_y,\rho,p)$. Similarly, to the upper one, the parameters were calculated at the lower boundary of the computational domain.

The no-slip conditions and thermal insulation of the walls were used on the solid surface.

2.3 Computational Domain

As a streamlined body, the wing profile NACA0012 with a chord of 1 m was taken (Fig. 1). Equations (1-4) were solved in dimensionless form. The scales used were: for linear parameters, the value of the chord of the wing profile, for velocities, the value of the longitudinal velocity vector component at the left boundary, for pressure and density, the values of pressure and density corresponding to $u_{x\infty}$.

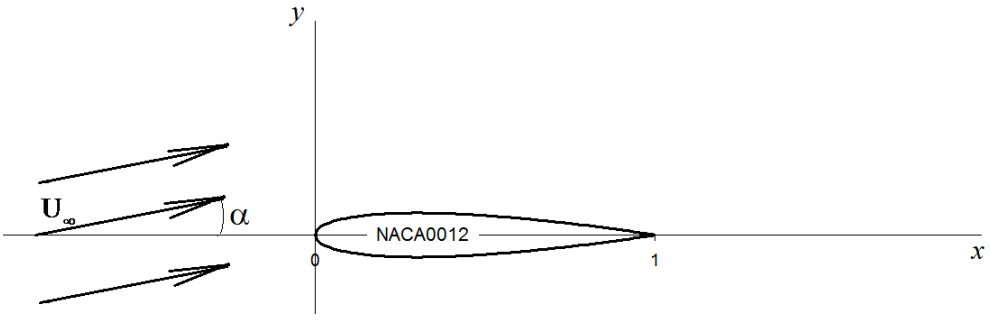

Figure 1 – Computational domain.

The calculations of the unsteady flow around the wing profile were carried out for the computational domain with dimensions: $x \in [-2,5]$, $y \in [-1,3]$. The computational domain was covered with a dense grid containing 16 800 000 points. In the vicinity of the streamlined body in the area $x \in [-0.1,1.5]$, $y \in [-0.08,1.5]$, the mesh was uniform. The grid step was 0.0002. With distance from the indicated area, the step increased linearly. Such a grid made it possible to calculate not only large-scale eddies, but also small structures in the near-boundary zone of a streamlined body, where dissipative terms play a significant role. The thinning of the grid near the boundary increased the numerical viscosity, which made it possible to smooth out the disturbances. At the same time, special nonreflecting boundary conditions made it possible to bring the perturbations out of the computational domain as correctly as possible. It should be noted that the applied conditions were not absolutely "absorbing", however, reflections from the boundaries did not fall into the region of the investigated body, but were carried away by the flow downstream. The dimensions of the computational region, at which reflections do not affect the solution near the streamlined airfoil, were obtained by methodological calculations. Thus, the obtained parameters on the profile were independent of the boundary reflections.

The calculations were carried out on the URAN multiprocessor computer system (IMM UB RAS) using the MPI parallelization technology.

3. Results and Discussion

The numerical results for the flow around the airfoil with the parameters $M = 0.7, Re = 2.63 \cdot 10^6$ were compared with the experimental data on for the pressure coefficient given in [8] (Fig. 2).

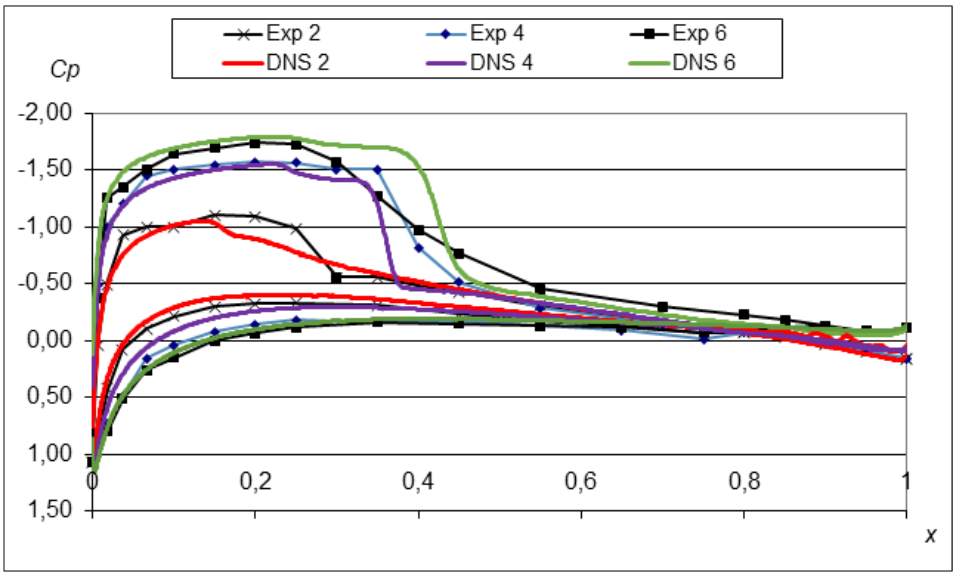

Figure 2 – Pressure coefficient on the NACA0012 profile (on the lower and upper surfaces) at attack angles of 2, 4 and 6 degrees, experimental and numerical data.

It is seen that the agreement between calculation and experiment is satisfactory. It should be noted that two-dimensional calculations give somewhat overestimated values for the pressure coefficient.

Calculations of hydromechanical parameters (HMP) for the wing profile of NACA0012 at $M = 0.7, Re = 2.63 \cdot 10^6$ were carried out for attack angles, varying from 2 to 8 degrees. In Fig. 3 shows Schlieren image of the averaged longitudinal component velocity vector field for the attack angle $\alpha = 5^\circ$. Calculations show that at $\alpha = 2^\circ$, a weak shock wave is formed on the wing leeward side at $x = 0.18$. At the same time, a low pressure zone (Fig. 4) and high flow velocities begins to form in the forward part of the wing leeward side.

With an increase in α, the pressure in the front part vicinity of the profile on its leeward side drops sharply, and then increases sharply at $x \geq 0.4$. In this place (the point $x = 0.4$ vicinity), λ-shaped

shock wave is formed. When passing through this shock wave, the flow velocity decreases and the pressure increases. With increasing α, the shock wave moves downstream. When $\alpha = 5^\circ$ the "leg" of the λ-shaped shock wave is strongly blurred, and when $\alpha = 6^\circ$ it disappears. The location of the shock wave is stabilized at $x = 0.4$. In this case (Fig. 4), along with an α increase, the pressure in the front part of the wing profile leeward side increases, and the flow velocity along the length of the wing leeward side is leveled, and the shock wave is smeared out.

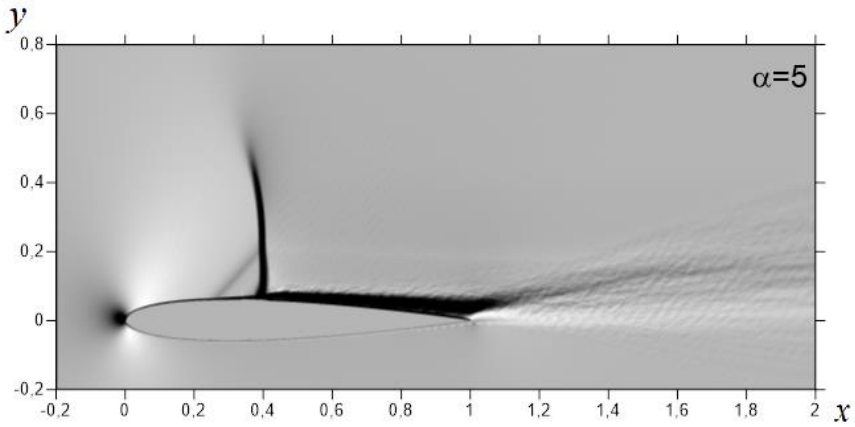

Figure 3 – Schlieren image of the averaged longitudinal velocity component field.

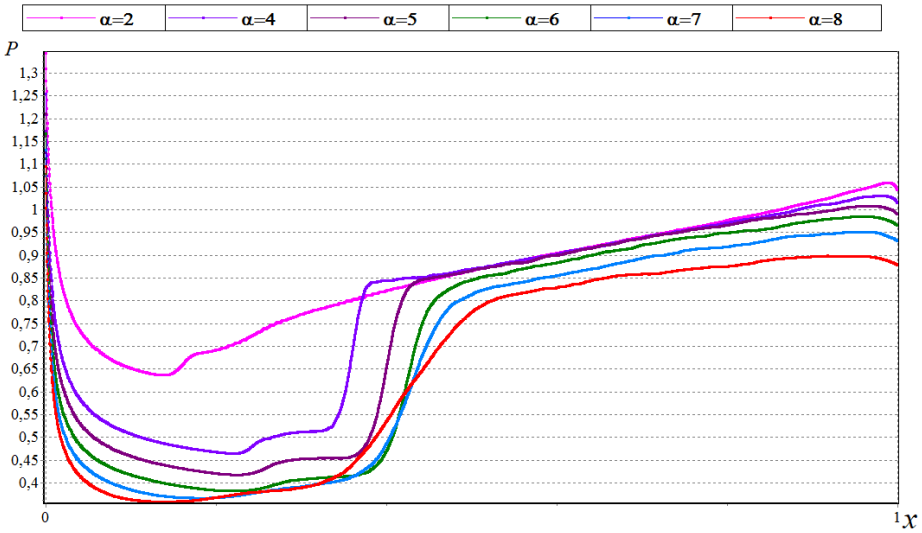

Figure 4 – Average pressure distribution on the wing profile leeward side.

In Fig. 5 shows the curves of the lift coefficients values C_L depending on time and for different attack angles. With the attack angle increase, the C_L values experience more and more intense pulsations with a frequency of about three oscillations per unit of dimensionless time, which corresponds to a frequency of 130 *Hz*. The C_L averaged values also begin to fluctuate, although at a significantly lower frequency. We can talk about the high-speed buffet onset at attack angles above 7 degrees, when the averaged parameters begin to fluctuate according to a law close to harmonic.

The shock wave location on the leeward side corresponds to the maximum pulsation values of HMP. This is clearly seen in the example of pressure deviations (Fig. 6) from their average values for the corresponding attack angles α shown in Fig. 4. Here (Fig. 6) shows the standard deviations σ equal to

$$\sigma_p = \frac{\delta p}{\bar{p}} = \frac{\sqrt{\frac{1}{n-1}\sum_1^n \left(p^i - \bar{p}\right)^2}}{\bar{p}}.$$

It can be seen that the $\delta p / \bar{p}$ maximum corresponds exactly to the $x \approx 0.4$ coordinate where the

shock wave is located. And at first it moves downstream with the shock wave, and then returns again to the $x = 0.4$ coordinate with the shock wave.

With an attack angle increase, the $\delta p / \bar{p}$ value only increases monotonically. The dependence of this value along the coordinate is more complex. Downstream, it sharply (by half) decreases and starts to grow again only at the wing profile trailing edge in the presence of the flow separation.

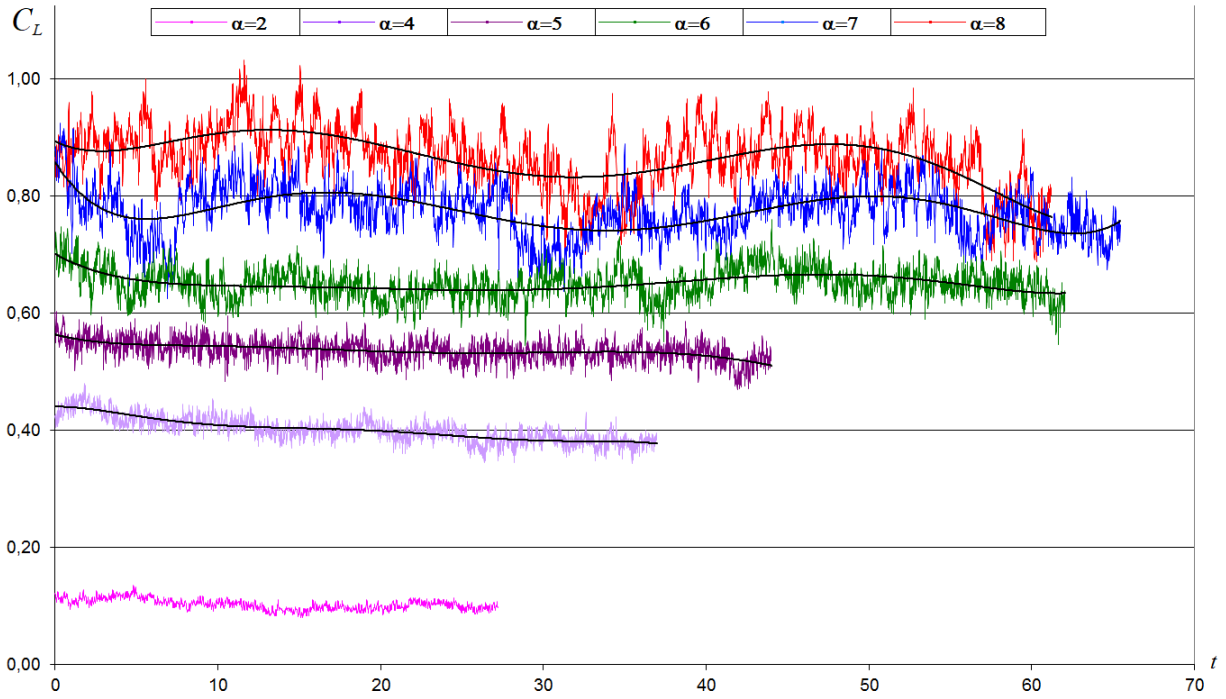

Figure 5 – Dependence of the lift coefficients on the dimensionless time.

It can be said that at attack angles equal to 7 and 8 degrees, oscillatory processes occur along most of the wing leeward surface, starting from $x = 0.1$. In the shock wave located area oscillatory phenomena are especially intense and dangerous for the aircraft structure. Therefore, it can be concluded that at attack angles equal to 7 and 8 degrees, high-speed buffet takes place, accompanied by intense oscillatory processes.

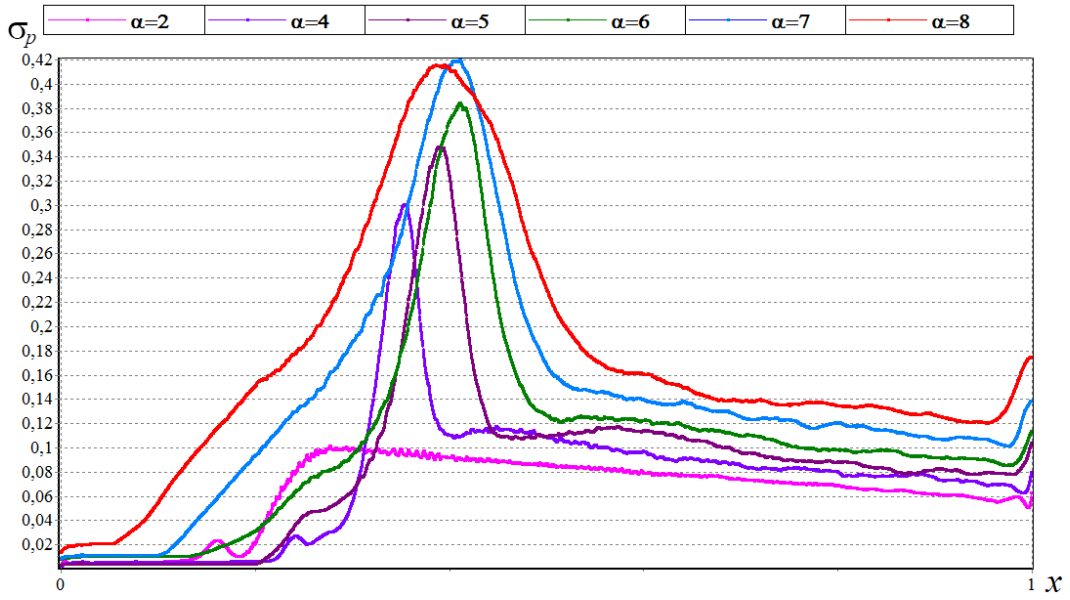

Figure 6 – Distribution of pressure pulsations on the wing profile leeward side.

Some more figures are shown for the flow velocity vector longitudinal component fields at $\alpha = 2^\circ$ (Fig. 7) and $\alpha = 8^\circ$, when the coefficients C_L and C_D (drag coefficient) have a local minimum and maximum (Fig. 8). When $\alpha = 2^\circ$ (Fig. 7), it is seen that after $x = 0.4$ the flow detaches from the wing profile surface and, in the form of separate vortices of the "Karman chain" type, leaves its trailing edge. In Fig. 7, a λ-shaped shock wave and a large number of discontinuities of the flow velocity vector longitudinal component are seen, extending upward from the wing profile.

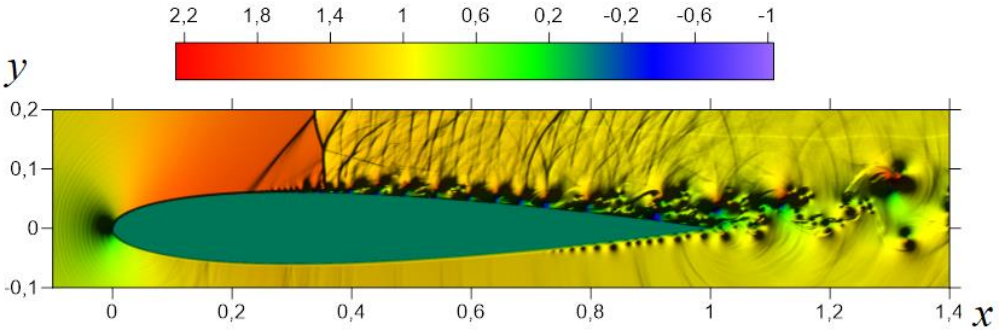

Figure 7 – Longitudinal velocity component pattern, $\alpha = 2^\circ$.

At $\alpha = 8^\circ$ (Fig. 8*a*, minimum for the coefficients C_L and C_D), there is a significantly increased separation zone located downstream of the coordinate $x = 0.4$. The zone of velocity longitudinal component perturbations extends upstream approximately to the coordinate $x = 0.2$ and ends with an oblique shock. Downstream, the vortex field occupies a fairly wide strip, and in the direction of the wing profile normal it contains many curvilinear intersecting oblique shocks. All this vortex structure flows down from the wing profile.

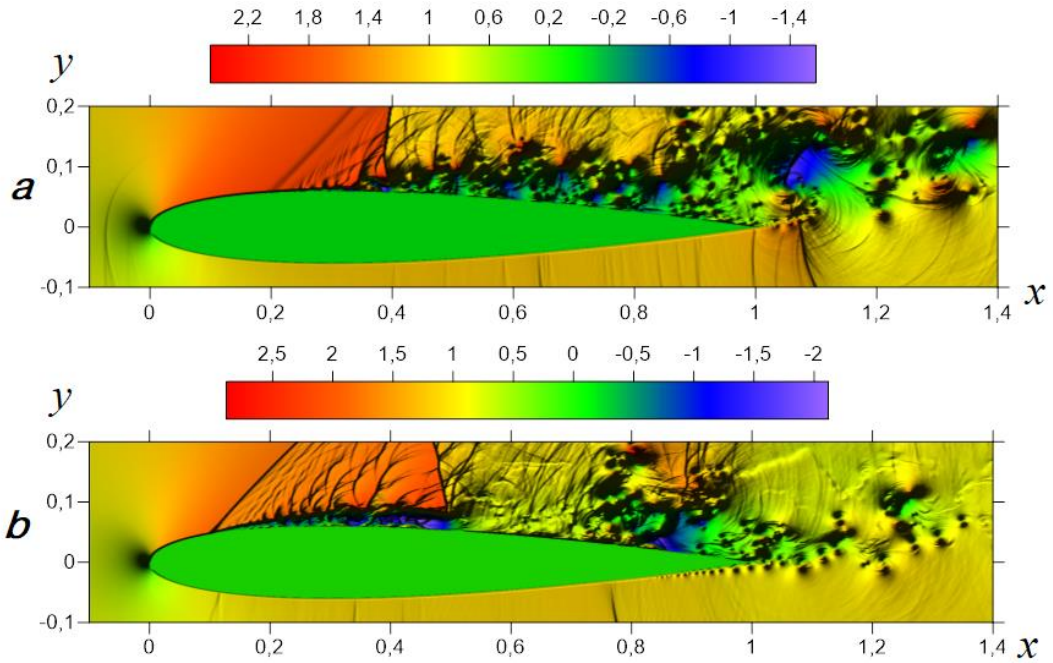

Figure 8 – Longitudinal velocity component pattern, $\alpha = 8^\circ$
(*a* - C_L and C_D minimum, *b* - C_L and C_D maximum).

For angles of attack corresponding to the maximum of the C_L and C_D coefficients (Fig. 8*b*), there is a separation zone displaced upstream to the coordinate $x = 0.1$, and, as in the case of minima of the coefficients, a wide vortex strip flowing downstream from the wing profile. The field of the flow velocity vector longitudinal component on the left ends with an oblique shock starting at $x = 0.1$, and has a complex structure containing a system of branching and intersecting oblique shocks. Since

the maxima and minima of the C_L and C_D coefficients are repeated in time with a certain frequency, the separation zone on the wing profile leeward side performs reciprocating movements. This indicates the buffet onset, (a process of intensive change in parameters with cycles repeating in time).

In fig. 9 shows the power spectral density S of the lift coefficient for small attack angles (two, four and five degrees). Spectral density is concentrated only at low frequencies and has a small value. In fig. 10 shows the power spectral density for large attack angles. It is seen that with increasing α, the spectral density increases. At angles above seven degrees, oscillations occur at higher frequencies. On the graph for eight degrees, this is most clearly discernible. For attack angles above seven degrees it can be said about the presence of aerodynamic forces self-oscillations and the occurrence of the high-speed buffet onset phenomenon.

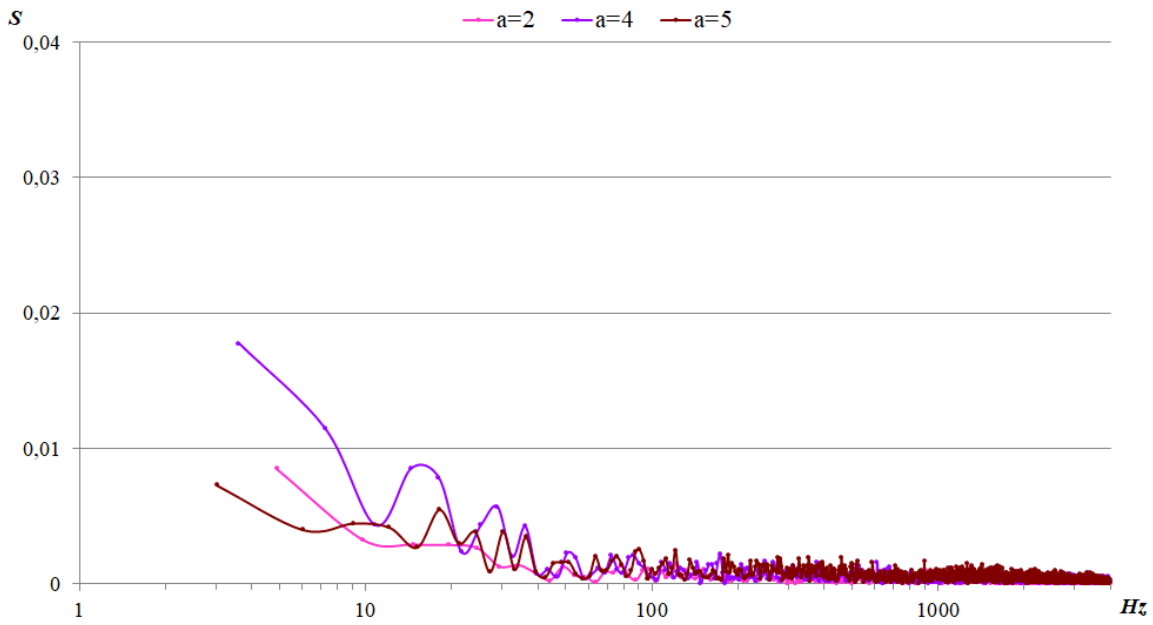

Figure 9 – Power spectral density of lift coefficient for small attack angles.

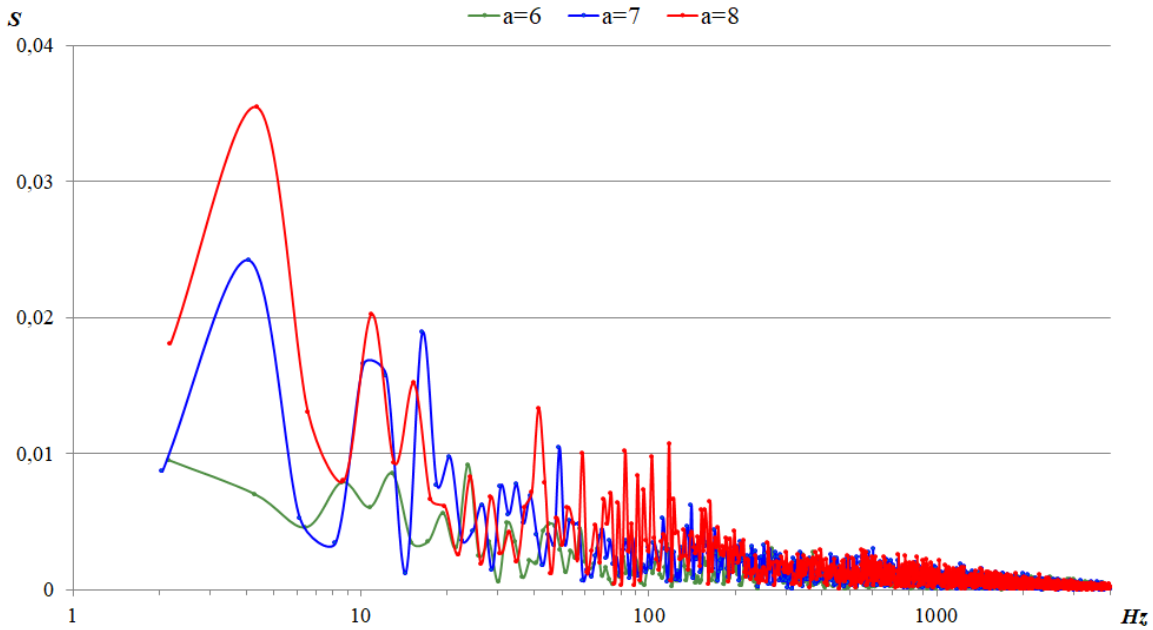

Figure 10 – Power spectral density of lift coefficient for large attack angles.

4. Contact Author Email Address

mailto: igor_lipatov@mail.ru

5. Copyright Statement

References

[1] Fam T.V. *Numerical simulation of the buffet onset in the transonic flow and methods of buffet controlling*, Cand. Sci. (Phys.-Math.) Dissertation, Zhukovsky, 2014, 123 p. (In Russian).

[2] Elizarova T.G., Chetverushkin B.N. Kinetic algorithms for calculating gas dynamic flows. *Computational Mathematics and Mathematical Physics*, Vol. 25, No. 5, pp. 164–169, 1985.

[3] Chetverushkin B.N. *Kinetically consistent schemes in gas dynamics:a new viscous gas model, algorithms, parallel implementation, applications.* Moscow: MoscowState University, 1999.

[4] Chetverushkin B.N. Kinetic schemes and high-performance multiprocessing calculations in gas dynamics. *Computational Technologies*, Vol. 7, No. 6, pp. 65–89, 2002.

[5] Gottlieb S., Shu C.-W. Total variation diminishing Runge–Kutta schemes. *Mathematics of Computation*, Vol. 67, No. 221, pp. 73–85, 1998.

[6] Liu X-D., Osher S., Chan T. Weighted essentially non-oscillatory schemes. Journal of Computational Physics, Vol. 115, No. 1,pp. 200-2012, 1994.

[7] Dorodnicyn L.V. Nonreflecting boundary conditions and numerical simulation of external flows. *Computational Mathematics and Mathematical Physics*, Vol. 51, No. 1, pp. 143-159, 2011.

[8] Braza M. NACA0012 with Aileron. *Unsteady effects of shock wave induced separation*, Berlin: Springer, pp. 101–131, 2011.